PARAGENESIS AND COMPOSITION OF TOURMALINE TYPES ALONG THE P2 FAULT AND MCARTHUR RIVER URANIUM DEPOSIT, ATHABASCA BASIN, CANADA

Erin E. Adlakha and Keiko Hattori

Department of Earth Sciences, University of Ottawa, Ottawa, Ontario, K1N6N5, Canada

Abstract

The P2 fault, a 13 km-long steeply dipping reverse fault, is the main structural control of the McArthur River uranium deposit in the eastern Athabasca Basin, northern Saskatchewan, Canada. Three types of tourmaline were observed in the metasedimentary basement rocks along the P2 fault: early oxy-schörl [$(Na_{0.47}\square_{0.37}Ca_{0.16})(Fe^{2+}_{1.30}Al_{0.91}Mg_{0.72}Ti_{0.07})$ $Al_6(Si_{5.79}Al_{0.21}O_{18})(BO_3)_3OH_3(O_{0.63}OH_{0.29}F_{0.08})$, where $\square$ = vacancy] of metamorphic-anatectic origin, hydrothermal oxy-dravite [$(Na_{0.57}Ca_{0.23}\square_{0.18}K_{0.02})(Mg_{1.93}Fe^{2+}_{0.62}Al_{0.29}Ti_{0.15})Al_6(Si_{5.93}Al_{0.07}O_{18})(BO_3)_3OH_3(O_{0.57}OH_{0.23}F_{0.20})$], and magnesio-foitite [$(\square_{0.77}Na_{0.20}Ca_{0.02}K_{0.01})(Mg_{1.99}Al_{0.92}Fe^{3+}_{0.07})Al_6(Si_6O_{18})(BO_3)_3(OH_3)(OH_{0.71}O_{0.25}F_{0.04})$]. Oxy-schörl formed in granitic pegmatites, a partial melt product of the metasediments during peak metamorphism. Oxy-dravite formed from hydrothermal fluids after the peak metamorphism but before deposition of the Athabasca sandstones, whereas magnesio-foitite is a product of later, low-temperature hydrothermal activity. Both oxy-schörl and oxy-dravite are coarse-grained (from 500 μm up to 1 cm), whereas magnesio-foitite occurs as radial aggregates of fine, prismatic crystals (<15 μm in width). Magnesio-foitite crystallized together with sudoite, illite, and "APS" minerals (alunite supergroup LREE-rich aluminum phosphate-sulfate minerals) along the entire studied length (∼7 km) of the P2 fault and is abundant in proximity to the Zone 2 ore body of the McArthur River deposit. In the ore zone, the assemblage occurs with uraninite and is partially overprinted by late, remobilized uraninite and sudoite. Therefore, magnesio-foitite is likely contemporaneous with the main stage of uranium mineralization. It is characterized by a high vacancy at its X-site (0.70–0.85 *apfu*) and high Al at its Y-site (0.70–1.12 *apfu*), suggesting that magnesio-foitite likely replaced pre-existing high-Al phases, such as kaolin and sudoite. The occurrence of magnesio-foitite along the entire P2 fault, in both areas of mineralization and apparently barren areas, suggests chemically similar fluids travelled along the entire P2 fault, but only produced ore in localized areas.

Keywords: tourmaline, oxy-schorl, oxy-dravite, magnesio-foitite, unconformity-type uranium deposits, hydrothermal ore deposits, alteration.

Introduction

The Proterozoic Athabasca Basin hosts world-class unconformity-type uranium deposits, including the McArthur River deposit. Prevalent models for uranium mineralization invoke an oxidizing, highly saline brine (25–35 wt.% NaCl equiv.), with a marine component, generated during basin development (*e.g.*, Hoeve & Sibbald 1978, Kotzer & Kyser 1995, Alexandre *et al.* 2005, Derome *et al.* 2005, Richard *et al.* 2011, Mercadier *et al.* 2012). Quartz-hosted fluid inclusions in ore breccias indicate that two types of fluids were present during mineralization: (1) an earlier, acidic, NaCl-rich, uranium-bearing brine and (2) an evolved CaCl₂-rich brine assumed to have formed through the interaction of the earlier brine with unconformably underlying basement rocks (Derome *et al.* 2005, Richard *et al.* 2010, Richard *et al.* 2011, Richard *et al.* 2012). Uranium deposition was caused by the reduction of U^{6+} to U^{4+} in the fluids. Proposed reductants include minerals (*e.g.*, graphite, Fe^{2+}-bearing chlorite and sulfides) within the basement rocks and faults (*e.g.*, Hoeve & Sibbald 1978, Alexandre *et al.* 2005) and reducing fluids released from the basement (Hoeve & Sibbald 1978, Hoeve & Quirt 1984, Kotzer & Kyser 1995, Kyser *et al.* 2000, Alexandre *et al.* 2005).

The uranium deposits commonly occur at the intersection of the unconformity with basement faults

along graphite-bearing pelitic rocks (*e.g.*, the P2 fault of the McArthur River deposit). Considering the spatial association of basement faults with mineralization, the faults are assumed to have acted as conduits for ore-fluids of either basin or basement origin (*e.g.*, Hoeve & Quirt 1984). Detailed petrographic work on basement rocks along the faults is lacking; therefore, the exact role of the faults during mineralization is not well understood.

Hydrothermal tourmaline is ubiquitous in close proximity to the Athabascan uranium deposits (*e.g.*, Hoeve & Sibbald 1978, Alexandre *et al.* 2005, Rosenberg & Foit 2006, Cloutier *et al.* 2009, Mercadier *et al.* 2012), but it is not common in other uranium deposit types. No tourmaline has been reported from unconformity-type uranium deposits in the Thelon Basin in northern Canada and the East Alligator Rivers district in northern Australia, both of which are considered to be similar in age and genesis to the deposits of the Athabasca Basin. Reported occurrences of tourmaline in uranium deposits are few, including the Mortimer Hills granitic pegmatite (Carter 1984) and the Jaduguda vein-type uranium (-Cu-Fe) deposit, India (Pal *et al.* 2010).

Tourmaline can accommodate many elements in its crystal structure (*e.g.*, Hawthorne & Dirlam 2011), therefore, its composition is useful in evaluating the geological environments from which it crystallized (*e.g.*, Copjakova *et al.* 2013, 2015). Two types of tourmaline have been reported in proximity to uranium deposits of the Athabasca Basin: an early dravitic tourmaline that occurs in the basement and as detrital grains in the sandstones of the Basin, and a later, hydrothermal alkali-deficient tourmaline (*e.g.*, Rosenberg & Foit 2006, Mercadier *et al.* 2012, Ng *et al.* 2013). The timing of this later, hydrothermal tourmaline with respect to uranium deposition is unclear. Opinions range from pre-ore (Ng *et al.* 2013), to syn-ore (Hoeve & Sibbald 1978, Kotzer & Kyser 1995, Fayek & Kyser 1997, Derome *et al.* 2005, Mercadier *et al.* 2012), to post-ore crystallization (Alexandre *et al.* 2005). This paper presents the occurrence and compositions of tourmaline in basement rocks along the P2 fault, Athabasca Basin, and discusses (1) the timing and paragenesis of different types of tourmaline, (2) hydrothermal fluids responsible for tourmaline crystallization, and (3) role of the P2 fault during uranium mineralization. This information is useful in identifying fertile structures associated with uranium deposits.

GEOLOGICAL SETTING

Regional geology

The Paleo- to Mesoproterozoic Athabasca Basin is underlain by the Archean to Paleoproterozoic western Rae and eastern Hearne Provinces (Fig. 1A, B). The Hearne Province is comprised of four accreted domains: (from west to east) the Peter Lake Domain, the Virgin River Domain, the Mudjatik Domain, and the Wollaston Domain. The Paleoproterozoic Wollaston Domain is a NE-striking fold-thrust belt comprising Archean granitoids overlain by Paleoproterozoic metasediments of the Wollaston Group. The Wollaston Group hosts, or occurs immediately below, most uranium deposits of the eastern Athabasca Basin (Fig. 1B). It is a package of graphitic and non-graphitic pelite, semi-pelite, and paragneiss with lenses of minor calc-silicate, arkose, and quartzite (McGill *et al.* 1993), which was metamorphosed during the Trans-Hudson Orogeny (*ca.* 1.8–1.9 Ga; Lewry & Sibbald 1980) under upper amphibolite to lower granulite facies conditions (Annesley *et al.* 2005). Granitic pegmatite lenses in the metasedimentary rocks formed through local partial melting during peak metamorphism (Annesley *et al.* 2005). Since quartzite is resistant to weathering and erosion, it forms prominent "ridges", or paleo-topographic highs, which elevate the unconformity. It has been noted that many uranium deposits of the Athabasca Basin are spatially associated with quartzite ridges (Jefferson *et al.* 2007, Kerr 2010).

Substantial weathering or erosion of the basement rocks beginning at *ca.* 1.73 Ga occurred before the deposition of the Athabasca Group sandstones (Kyser *et al.* 2000). The basement rocks at and below the unconformity show a vertical alteration profile comprising an uppermost Bleached Zone of kaolinite and illite, a middle Red Zone of hematite and kaolinite, and a lower Green Zone of sudoite and illite (Macdonald 1985, Adlakha *et al.* 2014).

The Athabasca Basin is comprised of a succession of fluvial to shallow marine arenites preserved at a maximum thickness of 1500 m in the center of the basin (Ramaekers *et al.* 2007). At McArthur River, the Athabasca Group sandstones have a thickness of 500 m, and consist of quartz arenite and basal quartz-pebble conglomerate of the Read Formation (RF), and the overlying sandstones of the Manitou Falls Formation which comprises the Bird Member (MFb), Collins Member (MFc), and Dunlop Member (MFd) in ascending order (Ramaekers *et al.* 2007).

Geology of the McArthur River deposit and P2 reverse fault

The McArthur River deposit contains six ore bodies (Zones 1–4 and A–B) with a collective strike over 1700 m (Fig. 1C). Uranium mineralization is constrained to the intersection of the P2 fault and the unconformity between the underlying metamorphic
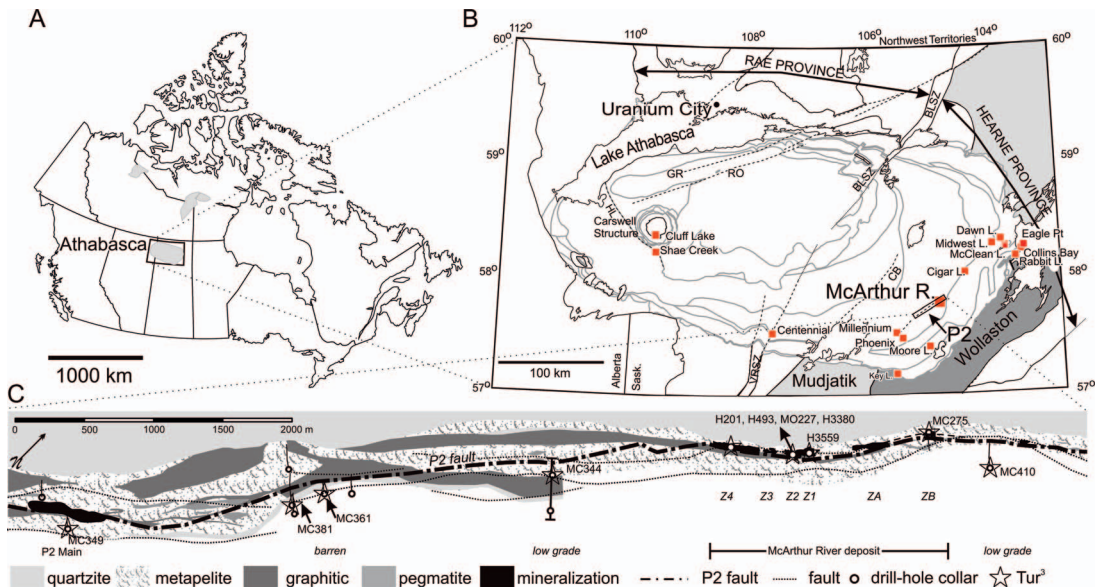
FIG. 1. (A) A map of Canada showing the location of the Athabasca Basin in Northern Saskatchewan. (B) A map showing the location of the major uranium deposits, including the McArthur River deposit, and structures, including the P2 fault, in the Athabasca Basin (modified from Jefferson *et al*. 2007). The southeastern margin of the Athabasca Basin is underlain by the Wollaston and Mudjatik Domains of the basement. Major shear zones: BLSZ= Black Lake, CB = Cable Bay, GR = Grease River, RO = Robbilard, VRSZ = Virgin River. (C) A schematic geological map of the basement rocks showing the P2 fault and the locations of sampled drill holes and mineralized zones. Drill holes in unmineralized areas occur along the southwest P2 fault and drill holes proximal to low-grade mineralization occur along the southwest and northeast portions of the P2 fault. Drill holes containing Tur3 (associated with U mineralization) are starred. Studied drill holes are labelled and correspond to the samples listed in Table 1. Z# = Zone # ore body. Modified from Adlakha & Hattori (2015).

rocks of the Wollaston Group and overlying sand-stones of the Athabasca Group. All ore bodies, with the exception of Zone 2, are hosted within the RF sandstone. The Zone 2 ore body is hosted predominately by graphitic pelites below the unconformity and is additionally bound by the Vertical Quartzite fault (VQ) to the west and faults striking 100–110° below the ore body. The VQ fault separates metapelites from a "quartzite ridge" near the unconformity (Fig. 1C). The ore bodies are enveloped by alteration haloes of sudoite, illite, tourmaline, and minor dickite (McGill *et al*. 1993).

The 13-km long P2 reverse fault, 040–045°/45°SE, is a broad deformation zone (McGill *et al*. 1993, Hajnal *et al*. 2007) along graphitic pelites that formed during the Trans-Hudson Orogeny (*ca*. 1.8–1.9 Ga; Lewry & Sibbald 1980). Reactivations of the fault produced splays in the Athabasca sandstones and resulted in the vertical displacement of the unconformity (up to 80 m) where the basement rocks were faulted over the lowermost sandstones (McGill *et al*. 1993). High-grade uranium mineralization of the

McArthur River deposit is found at the nose of the uplifted basement (all except Zone 2) or within the basement wedge of the P2 fault (Zone 2).

Relatively unaltered basement rocks occur >50 m from faults and the unconformity. They comprise garnet, biotite, feldspar, and quartz with or without pyrite, cordierite, graphite, and muscovite (Adlakha *et al*. 2014). They contain accessory zircon, monazite, and apatite and commonly show minor alteration whereby cordierite and biotite are replaced by chlorite and feldspar by illite. The mineralogy of relatively unaltered pegmatite is biotite, feldspar, and quartz with accessory zircon, monazite, and apatite and with or without muscovite, garnet, and pyrite.

The majority of rocks along the P2 fault are light green due to alteration forming sudoite (Al- and Mg-rich, di-trioctahedral chlorite), illite, tourmaline, sul-fides, and "APS" minerals (alunite supergroup LREE-rich aluminum phosphate sulfate minerals) (McGill *et al*. 1993, Adlakha *et al*. 2014, Adlakha & Hattori 2015). Rocks are locally stained red by hematite, or buff white (frequently termed "bleached") due to high

abundances of illite and/or kaolinite. Bleached rocks are common, especially in close proximity to mineralization and the unconformity (McGill *et al.* 1993). The area around the Zone 2 ore body is intensely altered to form sudoite and magnesio-foitite (Adlakha *et al.* 2014) and fault gouge is common.

Sampling and Methods

A total of 192 samples were collected from 27 drill cores along and within proximity to the P2 fault zone, extending from the McArthur River mine site to approximately 7 km southwest of it (Fig. 1). Most samples are hydrothermally altered metasedimentary rocks, pegmatite, and quartzite from the basement, with minor RF sandstone along the P2 fault. A total of 139 polished thin sections were made and then examined using a petrographic microscope with transmitted and reflected light sources.

Representative samples were selected for detailed mineralogical and textural analysis using a JEOL 6610LV scanning electron microscope at the University of Ottawa and carbon-coated sections because most alteration minerals are very fine-grained. Minerals were identified using energy-dispersive spectroscopy with a spectrum acquisition time of 40 s and an accelerating voltage of 20 kV.

Nineteen samples representing different environments were chosen for chemical analysis of tourmaline (Table 1): five samples (four basement, one RF sandstone) from barren areas of the P2 fault (from DDH MC361 and MC381; Fig. 1), four samples (three basement, one RF sandstone) from proximal (<20 m) to sandstone-hosted low-grade mineralization (from DDH MC370, MC349; Fig. 1), one sample from the basement below the Zone 1 ore body, seven samples from the Zone 2 ore body and associated alteration halo, and one sample of the Zone B ore body (MC274; Fig. 1). One sandstone sample of MFd was selected for comparison (MC274; Fig. 1).

Major and minor element abundance in tourmaline was quantitatively determined at the University of Ottawa using a JEOL 8230 electron-probe microanalyzer (EPMA) with an accelerating voltage of 15 kV, a beam current of 20 nA, and the beam focused to 5–10 μm in diameter depending on grain size. Data collection times for peak and background were 20 s for all elements except for K and Si (10 s), and F and Cl (50 s). The standards were as follows: sanidine (Si*K*α, Al*K*α, K*K*α), rutile (Ti*K*α), hematite (Fe*K*α), tephroite (Mn*K*α), sphalerite (Zn*L*α), diopside (Mg*K*α, Ca*K*α), albite (Na*K*α), tugtupite (Cl*K*α), sanbornite (Ba*L*α), fluorite (F*K*α), and celestine (Sr*L*α). Data reduction was carried out using a ZAF routine.

The chemical formula of tourmaline was calculated based on the ideal formula $XY_3Z_6(T_6O_{18})(BO_3)_3V_3W$, which assumes 3 B at the B site, 18 O forming the T site, and 3 OH at the V site (Tables 2 and 3). As suggested by Rosenberg & Foit (2006), the stoichiometric proportions of tourmaline were normalized to 15 cations (Y + Z + T sites). For cation site assignment, the T site was filled first with Si^{4+}, then Al^{3+} to sum 6 cations. The Z site was occupied by Al^{3+}, and the remaining Al^{3+} was assigned to the Y site. The Y site was filled by Ti^{4+}, Fe^{2+} or Fe^{3+}, and Mg^{2+}. All Ca^{2+}, K^+, and Na^+ were assigned to the X site. The W site accommodates F^-, OH^-, and O^{2-}. The proportions of OH^- and O^{2-} were calculated to compensate for excess cation charges. Iron was assumed to be Fe^{2+} for Tur1 and Tur2 (formula charge balance does not require Fe^{3+} which would further increase the already high $^WO^{2-}$) and Fe^{3+} for Tur3 (required due to the low sum of formula positive charges, resulting in an anion deficiency). The assignment of Fe^{2+} in Tur1 and Tur2 is supported by the following evidence: (1) the fO_2 is expected to be low in metapelites due to the buffer by abundant graphite, and (2) any Fe^{3+}, if present, is preferentially incorporated into co-existing muscovite and biotite over tourmaline (Dyar *et al.* 2002). Rosenberg & Foit (2006) also suggested Fe^{3+} for Tur3 due to the presence of abundant hematite in the hydrothermal assemblage.

Results

Tourmaline types and assemblages

Textural analysis indicates that three distinct types of tourmaline occur along the P2 fault. Tur1 is the least common tourmaline type and occurs only as relict grains (>2 mm), rimmed by Tur2, in a brecciated pegmatite lens (MAC85; Figs. 2A, 3A). It exhibits blue-green pleochroism under transmitted light microscope. It is difficult to evaluate the original mineral assemblage of Tur1, as it occurs as relict grains in altered pegmatite. However, the relict grains occur with plagioclase/feldspar, biotite, and quartz (Qz1, Table 1) that were pseudomorphically replaced by illite and chlorite. The texture suggests that plagioclase/feldspar, biotite, and quartz formed with Tur1.

Tur2 also occurs as relict grains and is most commonly found in altered pegmatite lenses and quartz-tourmaline veins in metapelites (Figs. 2B, 3A–C). Less commonly, Tur2 occurs as relict grains disseminated in altered metapelite (Fig. 3C, G). Tur2 is brown in hand specimens and exhibits brown-orange-yellow pleochroism in transmitted light (Fig. 3B, C). Tur2 forms subhedral–anhedral relict grains (0.2–2 mm) that display second-order birefringence

TABLE 1. SAMPLE DESCRIPTIONS

Area [a]	DDH	Sample	Rock type [a]	Depth (m) [b]	Proximity to ore	Tur occurrence	Mineralogy [c]
um	MC361	MAC109	pel/peg bx	587.6	>500 m	Tur2 100 μm–4 mm	Qz1, Qz2, Py1, Py2, Ilt1, Gr, Ms, Fe-ox, Sud1, Ilt2
	MC361	MAC110	pel bx	590	>500 m	Tur2 100 μm	Qz1, Gr, Py1, Ms, APS, Ilt2, Sud
	MC361	MAC111	peg	581.6	>500 m	Tur3 <50 μm Tur2 100 μm	Qz1, Gr, Py1, Py2 Qz2, Ms, Ilt1, Fe-ox, Kln, Ilt2, APS, Sud1
	MC361	MAC122	ss	493	>500 m	Tur3 vein 1 mm	Qz, Fe-ox, Kln, Ilt2, Sud1
	MC381	MAC436	peg	603	>500 m	Tur2 <100 μm Tur3 <50 μm	Qz1, Qz2, Ilt1, Gr, Ilt2, Sud, Rt
lg	MC370	MAC29	pel/peg bx	560.2	<1 m	Tur3 aggregates & disseminations	Qz1, Ap, Zr, Gr, Ms, Kln, Fe-ox1, Ilt2, Sud1 APS, Fe-ox
	MC370	MAC32	ss bx	543	20 m	Tur3 veinlets (<500 μm)	Qzd, Msd Zrd, Qz3, Kln, Il2, Sud1, APS
	MC349	MAC98	pel bx	578	<10 m	Tur2 100–200 μm Tur3 vein 300–500 μm	Qz1, Qz2, Fe-ox, U1, U2, Kln, Ilt2, Sud1
	MC349	MAC99	pel/peg bx	573	<10 m	Tur2 100–500 μm oriented vein Tur3 aggregates and veinlets <500 μm	Qz, Qz2, Py, Fe-ox, Ilt2, Sud, APS
Z1	H3559	MAC201	pel/peg bx	-	20 m	Tur2 <500 μm in Tur vein Tur3 aggregates <500 μm	Qz1, Qz2, Gr, Py1, Ms, Fe-ox, Ilt1, Sud1, Py2
Z2	H201	MAC69	pel	-	<20 m	Tur3 aggregates <500 μm	Qz1, Py1, Gr, Zr, Ilt1, Sud1, APS
	H201	MAC70	pel bx	-	<20 m	Tur3 aggregates <100 μm	Qz1?, Gr, Ilt2, Sud1
	H493	MAC85	peg/pel bx	-	20 m	Zoned Tur1 Tur2 1 mm Tur3 <10 μm	Qz1, Qz2, Py1, APS, Sud1, Ilt2
	H493	MAC86	pel bx	-	10 m	Tur3 aggregates 200 μm	Qz1?, Ms, Gr, Py1, Ilt2, Sud1
	MO227	MAC146	peg bx	-	n.d.	Tur3 vein 2 mm	Qz1, Gr, Py, Sud1, Ilt2, Fe-ox
	H3380	MAC423	pel	-	ore sample	Tur2 25 μm	Qz1, Bt, Qz2, Py1, Fe-Mg Chl, Ilt2, Sud1, U1, U2, Fe-ox, Py2 Sud2
	H3380	MAC425	pel	-	ore sample	Tur3 aggregates >500 μm Tur3 sphericules 100 μm	Qz1, Qz2, Ms, Fe-Mg Chl, Py1, Sud1, Ilt, U1, APS, U2, Py2
ZB	MC274	MAC440	ss	502.4	ore sample	Tur2 detrital Tur3 aggregates 150 μm	Qzd, Qz3, U1, Kln
MFd	MC274	MAC462	ss	93.1	>400 m	Tur3 aggregates 150 μm	Qzd, Qz3, Kln

a: um = unmineralized, lg = low grade, Z1 = Zone 1, Z2 = Zone 2, ZB = Zone B, MFd = Maitous Falls Formation D, bx = breccia, peg = pegmatitite, pel = pelite
b: sample depth in drill-hole collared from surface. Depths are not shown for underground collared drillholes.
c: Ap = apatite; APS = alumino-phosphate-sulphate minerals; Bt = biotite Clc = clinochlore; Dck = dickite; Fe-ox = clinochlore; Fe-Mg chl = Fe-Mg Chlorite; tg = fine-grained; Gr = graphite; Ms = muscovite; Ilt = illite; Py = pyrite; Qz = quartz; Sud = sudoite; U = uraninite; Xtm = xenotime; Zrn = zircon
"d" after mineral abbreviations indicates detrital mineral.

TABLE 2. AVERAGE COMPOSITIONS OF TUR1 AND TUR2

Sample	MAC85cores		MAC85rim		MAC99		MAC109		MAC111		MAC201	
Grains/pts	3/8		3/9		4/17		3/12		2/8		8/30	
	Tur1		Tur2		Tur2		Tur2		Tur2		Tur2	
	x̄	1σ	x̄	1σ	x̄	1σ	x̄	1σ	x̄	1σ	x̄	1σ
SiO_2	34.36	0.69	35.97	0.25	35.57	0.34	35.34	0.19	34.75	0.12	35.15	0.25
TiO_2	0.55	0.33	0.82	0.22	1.27	0.13	1.35	0.12	1.20	0.08	1.19	0.11
Al_2O_3	35.87	1.07	33.58	0.71	31.81	0.24	31.81	0.24	32.26	0.13	32.01	0.30
FeO	9.20	1.24	5.29	0.13	4.79	0.17	4.95	0.27	5.20	0.07	3.57	0.15
MnO	0.07	0.02	0.02	0.02	<0.01	0.02	0.03	0.01	0.02	0.01	<0.01	0.01
ZnO	0.07	0.02	0.04	0.02	<0.01	0.02	<0.01	0.01	0.02	0.03	<0.01	0.01
MgO	2.87	1.28	6.81	0.22	7.63	0.10	7.50	0.28	7.07	0.06	8.32	0.09
CaO	0.91	0.08	0.92	0.04	1.34	0.19	1.05	0.14	1.31	0.06	1.48	0.19
Na_2O	1.45	0.13	1.82	0.03	1.74	0.10	1.99	0.07	1.69	0.03	1.67	0.09
K_2O	0.05	0.01	0.05	0.01	0.07	0.01	0.07	0.01	0.08	0.01	0.07	0.01
F	0.15	0.07	0.40	0.05	0.53	0.08	0.24	0.07	0.42	0.08	0.45	0.06
Total	85.50	0.22	85.58	0.14	84.59	0.18	84.26	0.25	83.87	0.15	83.76	0.32

apfu

		MAC85cores		MAC85rim		MAC99		MAC109		MAC111		MAC201	
T	Si	5.79		5.95		5.97		5.94		5.88		5.91	
	Al	0.21		0.05		0.03		0.06		0.12		0.09	
Z	Al	6.00		6.00		6.00		6.00		6.00		6.00	
Y	Al	0.91		0.49		0.26		0.24		0.32		0.26	
	Ti	0.07		0.1		0.16		0.17		0.15		0.15	
	Fe^{2+}	1.30		0.73		0.67		0.70		0.74		0.50	
	Mg	0.72		1.68		1.91		1.88		1.79		2.09	
X	Ca	0.16		0.16		0.24		0.19		0.24		0.27	
	Na	0.47		0.58		0.56		0.65		0.56		0.54	
	K					0.02		0.01		0.02		0.02	
W	OH	0.29		0.26		0.12		0.32		0.22		0.19	
	O	0.63		0.53		0.60		0.55		0.55		0.57	
	F	0.08		0.21		0.28		0.13		0.23		0.24	

Notes: Stoichiometric proportions are normalized to 15 cations ($15 = T + Z + Y$) and 3B and 3OH per formula unit were assigned. BaO and SrO below detection limit of 0.01 wt.%.

colors. Tur2 is associated with quartz (Fig. 3B); it commonly occurs as anhedral grains interlocked or completely surrounded by quartz (Qz2, Table 1) or as subhedral grains in quartz veins. It also commonly contains quartz inclusions (Fig. 3B). Tur2 shows a close spatial association with graphite and pyrite where graphite forms elongated, micaceous grains that commonly wrap around Tur2 (Fig. 3C, G). Anhedral to euhedral pyrite (Py1, Table 1) occur in contact with Tur2 or quartz (Fig. 3A). The occurrence of Tur2 suggests that it formed in equilibrium with quartz, pyrite, and graphite. Some samples containing Tur2 contain relict biotite altered to "Fe-Mg chlorite" (intermediate composition between chamosite and clinochlore) and fine (<2 μm) to coarse-grained (>100 μm) illite (Fig. 3G). Fe-Mg chlorite and coarse-grained illite likely formed through the pseudomorphic replacement of earlier biotite or muscovite (Fig. 3G), although it is unclear whether this occurred

contemporaneously with Tur2. Fine-grained illite replaces feldspar (Adlakha et al. 2014). The mineral assemblages of Tur1 and Tur2 are partially overprinted by Tur3 and associated minerals and the rims of Tur2 grains are commonly altered to fine-grained Tur3.

Tur3 forms aggregates of fine, prismatic to acicular crystals (up to 15 μm in width and 5–500 μm in length), which are blue in hand specimen and colorless in thin section (Figs. 2C, 3B–D). The aggregates are disseminated in clay minerals and form monomineralic veinlets (up to 0.5 cm; Figs. 2C, 3C, D). Aggregates of Tur3 may pseudomorphically replace earlier Tur2 or form around Tur2 grains with their c-axis perpendicular to the rim of Tur2 (Fig. 3B, C). Along the P2 fault, Tur3 commonly occurs with sudoite (Sud1, Table 1), illite, and florencite-(Ce) (Fig. 3C, F–H; Table 1). The proportions of these minerals varies in locations: illite is predominant in barren areas of the P2 fault, whereas sudoite is abundant proximal to mineralized areas,
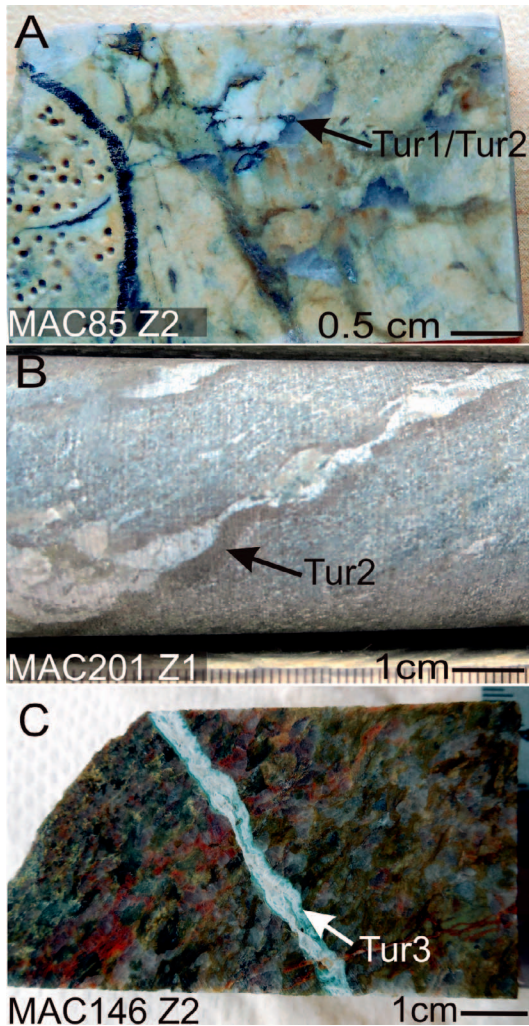
FIG. 2. Photographs of drill cores containing tourmaline. (A) Altered pegmatite (sample MAC85 from DDH H493 in Zone 2) containing zoned Tur1/Tur2; (B) tourmalinite (Tur2) vein in graphitic metapelite (sample MAC201 from DDH H3559 in Zone 1); (C) light blue Tur3 vein cross-cutting altered pegmatite (sample MAC146 from DDH H201 in Zone 2).

including low-grade and high-grade mineralization. Quartz appears to be in disequilibrium with Tur3 as it is resorbed in contact with Tur3 (Figs. 3B–D). Florencite occurs as small (<20 μm) pseudocubes (Adlakha & Hattori 2015).

Ore breccia from the Zone 2 ore body shows evidence for at least three distinct alteration events. The earliest event produced Tur2 with quartz, pyrite, graphite, Fe-Mg chlorite, and fine-grained illite. This assemblage is partially overprinted by uraninite (U1, Table 1), sudoite (Sud1), coarse-grained illite (>10 μm in length), euhedral florencite, and rosettes of Tur3 (Fig. 3F–G). The final event appears significantly late and affected only local areas. This is characterized by remobilized uraninite (U2) with sulfides (pyrite and lesser galena, Py2 in Table 1) and sudoite (Sud2) replacing Tur3 (Fig. 3E, F, H).

In the RF sandstones along the P2 fault, Tur2 occurs as detrital grains with quartz (Qz*d*, Table 1) and is overgrown by quartz (Qz3, Table 1), indicating that Tur2 formed before the deposition of the Athabasca sandstones. Tur3 in the RF forms monomineralic veinlets (MAC122; Fig. 3D; Table 1) or aggregates with sudoite, illite, and APS minerals between detrital quartz grains (MAC32; Table 1). In the MFd, Tur3 occurs in pore space and embays quartz overgrowths of detrital quartz grains (Fig. 3I).

Distribution of tourmaline types along the P2 fault

Tur3 is more abundant than Tur2 in the studied samples, although both types of tourmaline are found along the entire 7 km section of the P2 fault studied. Tur3 is concentrated in intensely altered basement rocks near and within the Zone 2 ore body of the McArthur River deposit (observed in 21 of 30 samples and represented by samples MAC69, MAC70, MAC86, MAC146, MAC423, MAC425). Tur3 is sparse in barren areas of the P2 fault in the basement (three of 18 barren samples and represented by MAC109, MAC110, and MAC111). Tur3 proximal to low-grade mineralization is found in the basement rocks along the P2 fault (MAC29, MAC98, MAC99) and within 5 m of the unconformity (four samples out of 13 proximal to low-grade mineralization contained Tur3).

For comparison, four tourmaline-bearing sandstones were studied. Three samples are of the lowermost RF sandstone from barren (MAC122), low-grade (MAC32), and mineralized (MAC440) areas of the P2 fault. The fourth sample (MAC462) is of the MFd sandstone directly above (>400 m) the Zone B deposit. Tur3 was observed in all four samples and Tur2 was observed in one sample of RF (MAC440). Tur1 was not observed in any of the sandstone samples.

Tourmaline composition

Tur1 is Fe-rich with an average formula of $(Na_{0.47}\square_{0.37}Ca_{0.16})(Fe^{2+}_{1.30}Al_{0.91}Mg_{0.7}Ti_{0.07})$ $Al_6(Si_{5.79}Al_{0.21}O_{18})(BO_3)_3OH_3(O_{0.63}OH_{0.29}F_{0.08})$ where $\square$ is a vacancy. It contains high Na (Fig. 4A) and shows considerable variations in Al (6.86–7.57

TABLE 3. AVERAGE COMPOSITIONS OF TUR3

Sample	MAC462		MAC110		MAC122		MAC436		MAC29		MAC32		MAC86		MAC99	
n[a]	9		11		3		10		4		11		20		2	
host rock[b]	MFd ss		pel		RF ss		pel		pel		RF ss		peg		peg/pel	
area[c]	above ZB		P2, barren		P2, barren		P2, barren		P2, lg		P2, lg		P2, lg		P2, lg	
	$\bar{x}$	1σ	$\bar{x}$	1σ	$\bar{x}$	1σ	$\bar{x}$	1σ	$\bar{x}$	1σ	$\bar{x}$	1σ	$\bar{x}$	1σ	$\bar{x}$	1σ
SiO_2	36.96	0.63	38.78	0.33	34.37	0.29	37.69	0.27	35.94	0.35	33.57	0.90	37.51	0.41	35.92	0.64
Al_2O_3	36.52	0.74	36.21	0.39	33.29	0.91	36.83	0.27	36.85	0.63	37.92	0.39	35.42	0.41	33.03	1.41
Fe_2O_3	0.21	0.04	1.71	0.70	2.33	0.22	0.54	0.17	1.35	0.08	0.87	0.13	0.14	0.04	1.68	0.13
MgO	8.09	0.14	8.34	0.33	6.96	0.04	8.29	0.30	7.88	0.12	7.41	0.13	8.58	0.16	7.14	0.13
CaO	0.13	0.01	0.03	0.01	0.05	0.01	0.10	0.02	0.09	0.01	0.23	0.04	0.08	0.04	0.07	0.01
Na_2O	0.80	0.10	0.49	0.10	0.83	0.07	0.67	0.05	0.55	0.08	0.50	0.07	0.71	0.14	0.70	0.08
K_2O	0.07	0.04	<0.01	<0.01	<0.01	<0.01	0.05	0.06	<0.01	<0.01	<0.01	<0.01	0.02	0.02	0.02	0.02
F	0.13	0.04	0.12	0.09	0.18	0.09	0.07	0.04	0.05	0.03	0.06	0.05	0.04	0.04	0.23	0.14
Total	82.85	0.89	85.36	0.29	77.77	0.93	84.21	0.37	82.64	0.43	80.48	0.79	82.50	0.46	78.47	2.41
FeO [d]	0.19	0.03	1.54	0.63	2.09	0.20	0.49	0.16	1.21	0.07	0.78	0.12	0.12	0.04	1.51	0.11
apfu																
T Si	6.01		6.11		6.01		6.02		5.85		5.60		6.11		6.21	
Al									0.15		0.40					
Z Al	6		6		6		6		6		6		6		6	
Y Al	1		0.72		0.86		0.94		0.92		1.05		0.79		0.73	
Mg	1.96		1.96		1.82		1.87		1.91		1.84		2.08		1.84	
Fe^{3+}	0.02		0.2		0.31		0.03		0.16		0.11		0.02		0.22	
X Na	0.25		0.15		0.28		0.21		0.17		0.16		0.23		0.23	
Ca	0.02				0.01		0.02		0.02		0.04		0.01		0.01	
K	0.01						0.01		0.00		0.00		0.00		0.01	
X-vac	0.72		0.85		0.71		0.76		0.81		0.80		0.76		0.75	
W F	0.07		0.06		0.10		0.04		0.03		0.03		0.02		0.13	
O	0.32		0.27		0.49				0.12		0.00		0.29		0.64	
OH	0.61		0.67		0.41		0.95		0.85		0.97		0.69		0.23	

Notes: a: number of analyzed grains; b: peg = pegmatite, pel = pelite, ss = sandstone; c: lg = lowgrade, Z1 = Zone 1, Z2 = Zone 2; d: Fe contents if total Fe is FeO. Stoichiometric proportions are normalized to 15 cations (15 = T + Z + Y); 3B and 3OH per formula unit were assigned. TiO_2, MnO, SrO, BaO, and Cl contents were below detection limit of 0.01 wt.%.

apfu), Fe (1.02–1.51 *apfu*), and Mg (0.34–1.17 *apfu*) (Table 2; Fig. 4).

Tur2 has an average composition of $(Na_{0.57} Ca_{0.23}\square_{0.18}K_{0.02})(Mg_{1.93}Fe^{2+}_{0.62}Al_{0.29}Ti_{0.15}) Al_6(Si_{5.93} Al_{0.07}O_{18})(BO_3)_3OH_3(O_{0.57}OH_{0.23}F_{0.20})$ with little compositional variation among grains ($n = 20$) from different samples (Table 2). The composition of Tur2 is similar along the P2 fault independent of the distance from mineralization (Fig. 4).

Tur3 has an average composition of $(\square_{0.77}Na_{0.20} Ca_{0.02}K_{0.01})(Mg_{1.99}Al_{0.92}Fe^{3+}_{0.07})Al_6(Si_6O_{18})(BO_3)_3 (OH_3)(OH_{0.71}O_{0.25}F_{0.04})$ (Table 3). Tur3 both in the basement and sandstones is alkali deficient with X-site vacancies ranging from 0.70–0.85 *apfu* (Fig. 4A; Table 3). With the exception of sample MAC425, Tur3 from individual samples are similar as indicated by the small standard deviations listed in Table 3. However,

Tur3 exhibits significant ranges in Mg (1.59–2.22 *apfu*) and Al (6.44–7.58 *apfu*) between samples (Fig. 4D). Tur3 from ore samples (MAC423 and MAC425 in Zone 2, and MAC440 in Zone B) exhibit uniformly high X-site vacancies (0.82–0.83 *apfu*). Tur3 from the barren areas of the P2 fault (samples MAC110, MAC122, MAC436) display a wide range (0.70–0.85 *apfu*) of X-site vacancies.

DISCUSSION

Evolution of tourmaline composition

The composition of Tur1 varies from oxy-schörl with high X-site vacancy (up to 0.4 *apfu*) to Mg-rich oxy-schörl with decreased vacancy at the X-site (Figs. 4A, C and 5A, B). The compositional variation of Tur1 is accompanied by a decrease of Al at the Y-site (Figs.

TABLE 3. CONTINUED.

Sample	MAC201		MAC69		MAC70		MAC146		MAC423		MAC425		MAC440	
n[a]	7		21		16		4		9		8		7	
host rock[b]	peg/pel		pel		pel		peg		pel		pel		RF ss	
area[c]	P2, Z1		P2, Z2		P2, Z2		P2, Z2		P2, Z2		P2, Z2		P2, ZB	
	x̄	1σ	x̄	1σ	x̄	1σ	x̄	1σ	x̄	1σ	x̄	1σ	x̄	1σ
SiO_2	37.44	0.19	36.60	0.59	36.73	0.70	35.03	1.22	37.52	0.94	36.70	1.09	37.37	0.19
Al_2O_3	34.50	0.84	35.50	0.45	35.80	0.53	34.85	0.88	36.22	1.05	37.13	1.58	36.78	0.81
Fe_2O_3	0.23	0.03	0.15	0.04	0.11	0.03	1.61	0.37	0.22	0.17	0.68	0.66	0.41	0.09
MgO	8.56	0.15	8.64	0.14	8.42	0.11	7.26	0.20	8.65	0.50	7.52	0.65	7.82	0.14
CaO	0.02	0.01	0.11	0.03	0.11	0.02	0.11	0.04	0.08	0.03	0.17	0.04	0.10	0.01
Na_2O	0.63	0.05	0.64	0.06	0.62	0.07	0.73	0.21	0.50	0.05	0.43	0.06	0.58	0.06
K_2O	<0.01	<0.01	0.03	0.02	0.04	0.05	0.02	0.02	0.04	0.03	0.08	0.07	<0.01	<0.01
F	0.04	0.05	0.08	0.04	0.06	0.04	0.04	0.02	<0.01	<0.01	0.03	0.04	0.09	0.05
Total	81.43	0.70	81.76	0.65	81.90	0.73	79.51	1.51	83.32	0.73	82.73	1.25	83.09	1.02
FeO [d]	0.21	0.03	0.13	0.03	0.10	0.03	1.45	0.33	0.19	0.15	0.65	0.56	0.37	0.08
apfu														
T Si	6.17		6.00		6.02		6.02		6.03		6.03		6.05	
Al														
Z Al	6		6		6		6		6		6		6	
Y Al	0.70		0.87		0.91		1.05		0.87		1.12		1.01	
Mg	2.10		2.11		2.06		1.86		2.07		1.76		1.89	
Fe^{3+}	0.03		0.02		0.01		0.07		0.03		0.09		0.05	
X Na	0.20		0.20		0.20		0.24		0.16		0.13		0.18	
Ca	0.00		0.02		0.02		0.02		0.01		0.03		0.02	
K	0.00		0.01		0.01		0.00		0.01		0.02			
X-vac	0.80		0.77		0.78		0.74		0.82		0.82		0.80	
W F	0.02		0.04		0.03		0.00		0.01		0.02		0.05	
O	0.28		0.14		0.20		0.43		0.15		0.48		0.38	
OH	0.70		0.82		0.77		0.57		0.84		0.50		0.57	

4B, C, and 5A) and an increase in F at the W site (Fig. 5C). The higher Mg and F and lower Al contents are characteristic of Tur 2, which sometimes overgrows Tur1; therefore, the Mg-enriched analyses of Tur1 most likely represent transitional compositions of mixed Tur1+Tur2 due to partial dissolution of Tur1 during crystallization of Tur2 around it (Fig. 3A). It is therefore reasonable to assume that Tur1 was originally relatively homogeneous oxy-schörl with high X-site vacancies.

The composition of Tur2 corresponds to oxy-dravite (Fig. 4C) and is similar between samples with small variations in Ca and F contents (Fig. 5). The Ca and F show a broad positive correlation which suggests a fluor-uvite component in the samples (Fig. 5D). Positive correlation between $Al^Y/(Al^Y + Mg + Fe)$ and X-site vacancy (Fig. 5A) and negative correlation between Mg/(Mg + Fe) and X-site vacancy (Fig. 5B) suggest a coupled substitution $Na^+ + Mg^{2+} = \square + Al^{3+}$.

The composition of Tur3 corresponds to magnesio-foitite (Fig. 4D) and is characterized by high Al and X-site vacancy (Fig. 5A). The data for Tur3 exhibit a positive correlation between Al content at the Y-site and X-site vacancy and a negative correlation between Mg/(Mg + Fe) at the Y-site and X-site vacancy. This suggests coupled substitution of $\square + Al^{3+} = Na^+ + Mg^{2+}$ (Fig. 5A, B). The F contents are variable from <0.01 to 0.22 *apfu* and inversely correlate with X-site vacancy (Fig. 5C). The F contents do not correlate with Ca contents, which range from <0.01 to 0.05 *apfu* (Fig. 5D). Tur3 also shows a large range in the ratio of O/OH at the W site (Fig. 4B) with an inverse correlation between Na^+ and OH^- (Fig. 5E), suggesting a probable solid solution of dominant magnesio-foitite with oxy-dravite *via* substitution $\square + OH^- = Na^+ + O^{2-}$. However, the small grain size of Tur3 resulted in low sums of oxides for the EPMA data (Table 3, see Supplementary data for full dataset). Since the OH and O contents are calculated based on charge balance, uncertainty in the EPMA data
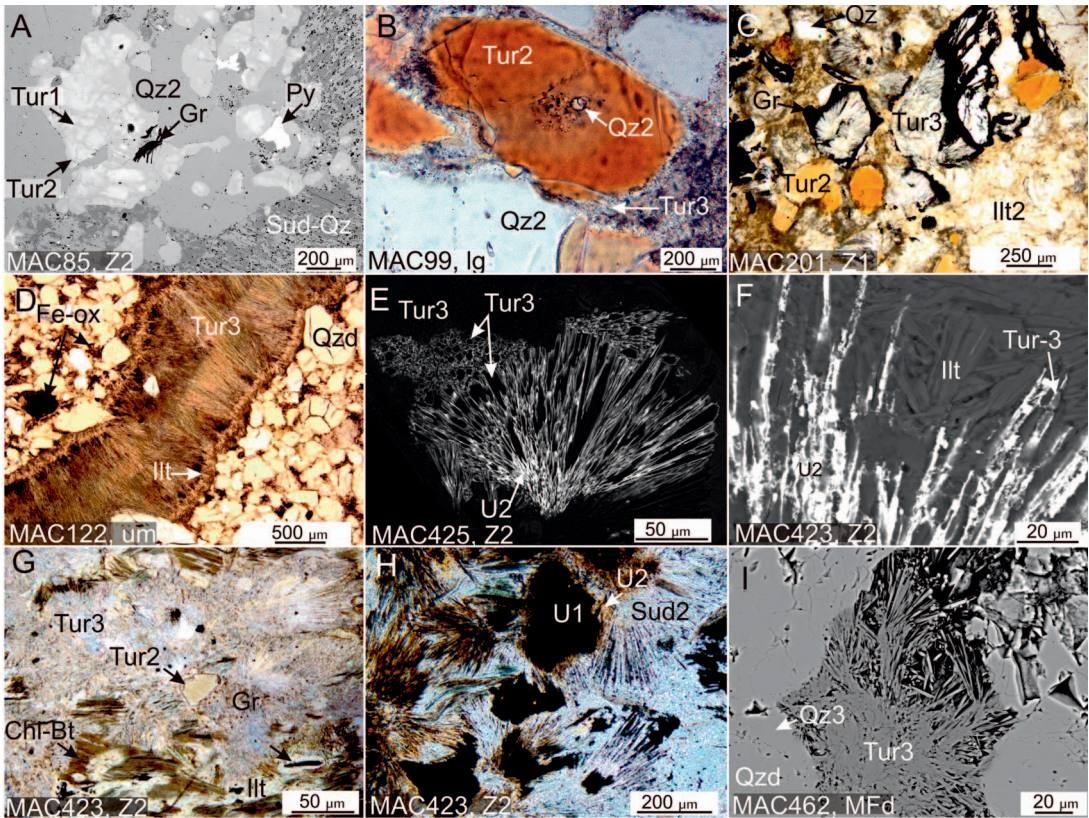
FIG. 3. Photomicrographs and back-scattered electron (BSE) images of tourmaline. (A) BSE image of rare zoned Tur2 with cores of Tur1 in pervasively altered pegmatite (sample MAC85 from DDH H493). (B) Tur2 containing quartz inclusions and rimmed by Tur3 in intensely altered metapelite proximal to low grade mineralization (sample 99 from DDH MC349). (C) Tur3 aggregates (likely pseudomorphs of earlier Tur2), partially resorbed Tur2 and quartz, and relict graphite (Gr) in illite (Ilt2) from intensely altered metapelite (sample 201 from DDH H3559) below the Zone 1 ore body. (D) Tur3 vein with marginal illite (Ilt) and Fe-oxide (Fe-ox) and partially resorbed quartz (Qz) in unmineralized (um) RF sandstone (sample MAC122 from MC361). (E) Tur3 aggregate overprinted by remobilized uraninite (U2) in Zone 2 ore breccia (sample MAC425 from DDH 3380). (F) Remobilized uraninite along grain boundaries between illite and Tur3. (G) An early assemblage of Tur2 with Fe-Mg chlorite (pseudomorphically replacing biotite; Chl-Bt), graphite, and pyrite overprinted by Tur3 with recrystallized illite (sample MAC425 from DDH 3380). (H) Brownish remobilized uraninite (U2) overprints opaque early uraninite (U1) and sudoite (Sud2) pseudomorphs of Tur3 (sample MAC423 from DDH H3380). (I) BSE image of Tur3 interstitial to detrital quartz (Qz1) overgrown by quartz (Qz3) in MFd sandstone above Zone B ore body (sample MAC462 from DDH MC274).

propagate uncertainty in the evaluation of OH and O. Therefore, the values of O/OH ratio at the W site should be taken with caution.

The low oxide sums for Tur3 and high Si contents (cation normalization on T+Z+Y=15 *apfu* commonly leads to a slight excess of Si, >6 *apfu*) might suggest the presence of other cations at the Y site. One possible cation is Li because it cannot be measured with EPMA. We consider high Li to be unlikely because Li-bearing tourmaline is not common outside Li-bearing pegmatites, although Richard *et al*. (2010)

reported high Li contents (10^2–10^4 ppm) in fluid inclusions in quartz associated with uranium mineralization.

Origin of Tur1 and Tur2

The presence of oxy-subgroup tourmaline in metamorphic rocks is well documented: oxy-schörl described by Bačík *et al*. (2013) occurs in metasomatically altered rhyolites from the Slovak Republic and in muscovite-tourmaline orthogneiss in the Czech Re-
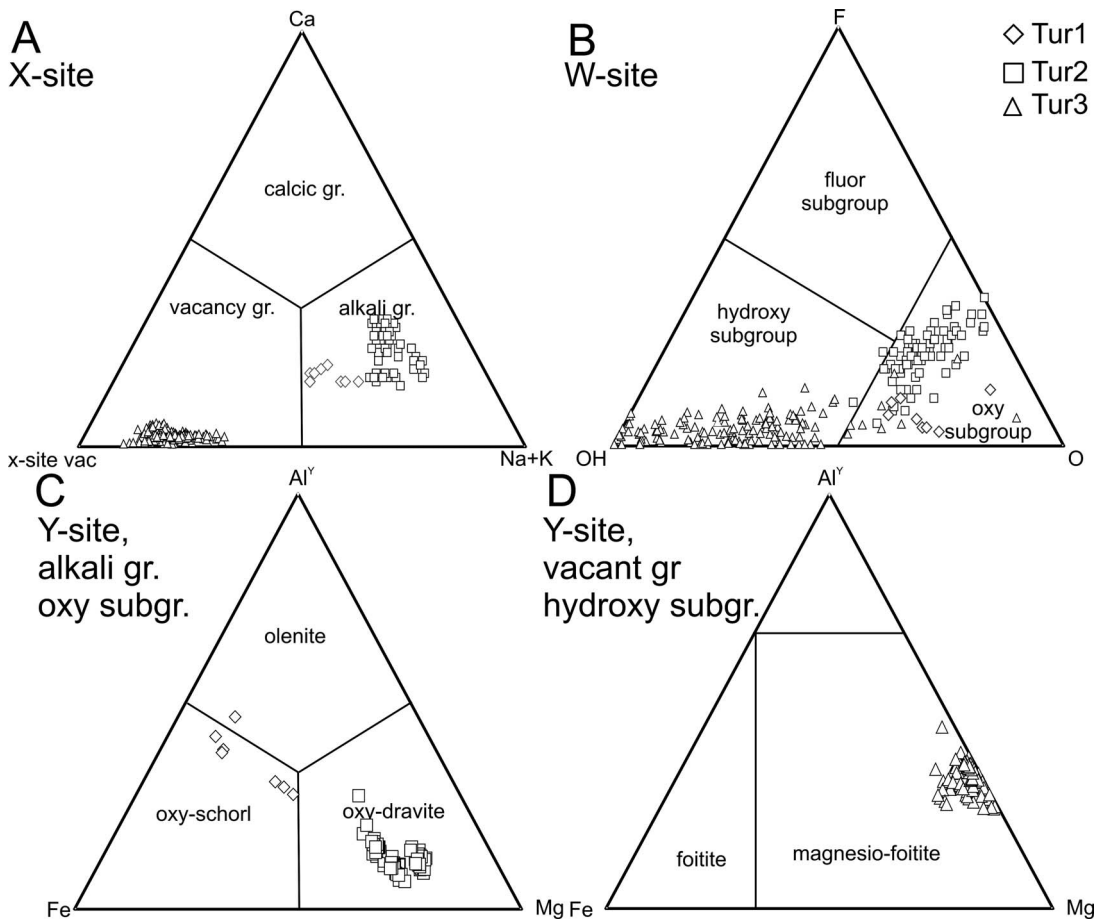
FIG. 4. Tourmaline classification ternaries (Henry *et al*. 2011). (A) X-site occupancy; (B) W-site occupancy; (C) Y-site occupancy for oxy species of alkali group; and (D) Y-site occupancy for hydroxy species of X-site vacant group.

public, whereas oxy-dravite occurs in quartz-muscovite schist of the Narok district, Kenya (Bosi & Skogby 2013) and in graphitic quartzite at Bítovánky, Czech Republic (Cempírek *et al*. 2013). Oxy-schörl and Fe-rich oxy-dravite have been reported in pegmatites from the Moldanubicum, Czech Republic, that are considered to be partial melts of metapelites (Novák *et al*. 2004), although Al-rich schörl and foitite are more common in pegmatites (Gadas *et al*. 2012).

In the tourmaline provenance diagram of Henry & Guidotti (1985), oxy-schörl (Tur1) examined in this study plots close to Fields 1 and 2 representing the composition of tourmaline in granitoid pegmatites (Fig. 6A). Our oxy-schörl occurs in altered pegmatite, which was originally composed of biotite, muscovite, feldspar, and quartz prior to hydrothermal alteration. The occurrence suggests it is indeed of magmatic

origin, and crystallized in pegmatites that are partial melt products of metasedimentary rocks.

Coarse-grained dravitic tourmaline has been previously reported in the basement (Rosenberg & Foit 2006, Mercadier *et al*. 2012) and is similar in composition to the oxy-dravite (Tur2) described in this study (Fig. 6A). Mercadier *et al*. (2012) also reported zoned dravitic tourmaline with schörlitic cores in basement pegmatite, similar in composition to the zoned Tur2 of this study (Fig. 3A). The dravite occurs in the Eagle Point uranium deposit (Mercadier *et al*. 2012), the Second Link Lake deposit, and the Rabbit Lake deposit (Rosenberg & Foit 2006), all of which occur in reactivated Hudsonian deformation zones (Hoeve & Sibbald 1978). Tourmaline similar to the composition of Tur2 also occurs as detrital grains in the Athabasca sandstones (*e.g*., Quirt *et al*. 1991, Rosenberg & Foit 2006, Mercadier *et al*. 2012, Ng *et*
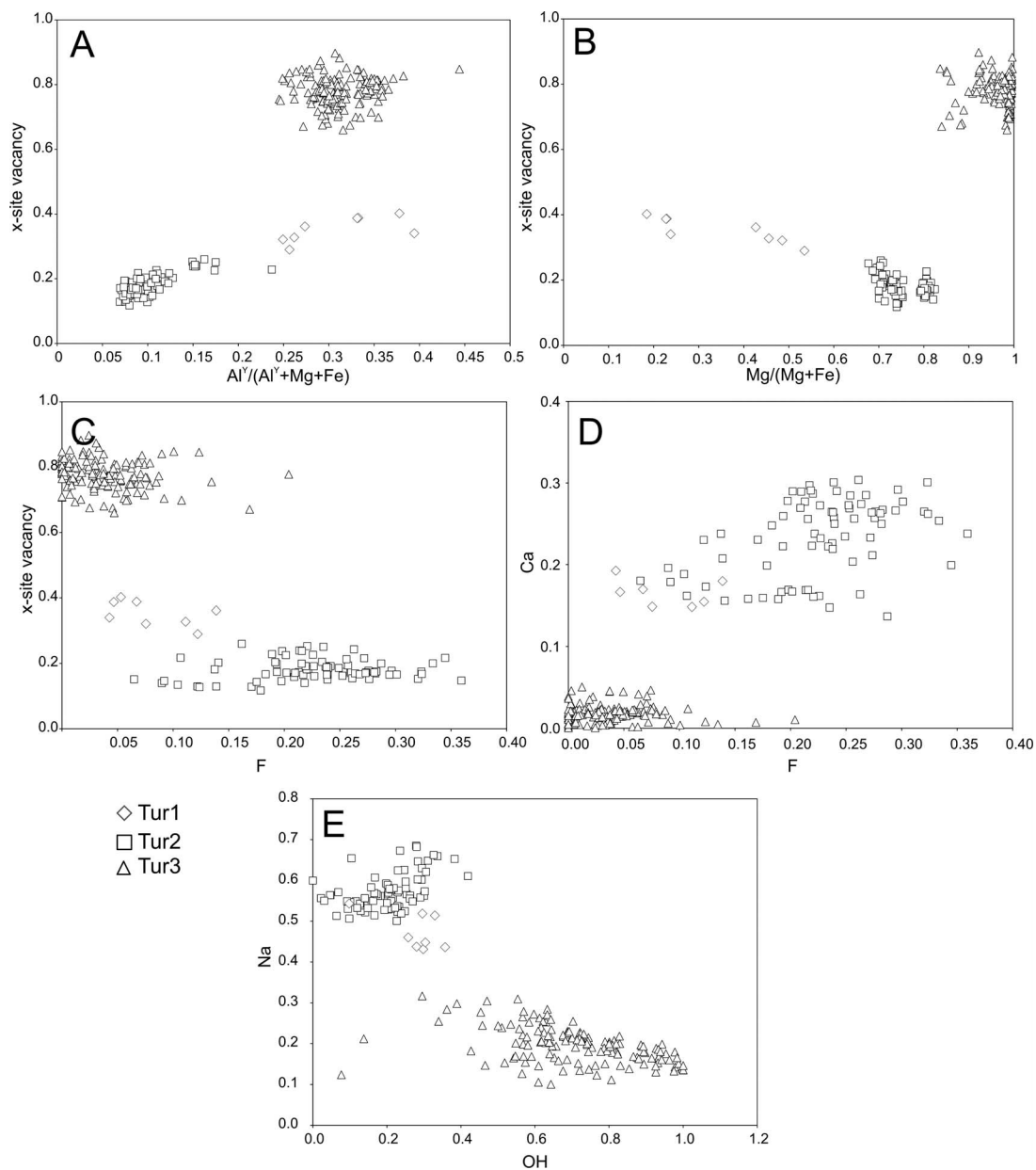
F ɪɢ. 5. Binary plots displaying (A) $Al^Y/(Al^Y + Mg + Fe)$ *versus* X-site vacancy, (B) $Mg/(Mg + Fe)$ *versus* X-site vacancy, (C) F *versus* X-site vacancy, (D) F *versus* Ca, and (E) OH *versus* Na in Tur1 (diamonds), Tur2 (squares), and Tur3 (triangles). All data are calculated as atoms per formula unit.

al. 2013, this study; Fig. 4B), confirming crystallization before deposition of the Athabasca Basin.

The origin of this oxy-dravite is debated as to whether it is a metamorphic product (Adlakha *et al.* 2014) or a crystallization product of partial melts (Mercadier *et al.* 2012). Oxy-dravite of this study plots

in Field 4 of the provenance diagram (Fig. 6A), suggesting its formation during metamorphism. However, oxy-dravite occurs in high abundance in pegmatite samples, which suggests its crystallization from a partial melt. As mentioned, Fe-rich oxy-dravite has been reported from pegmatites in the Czech
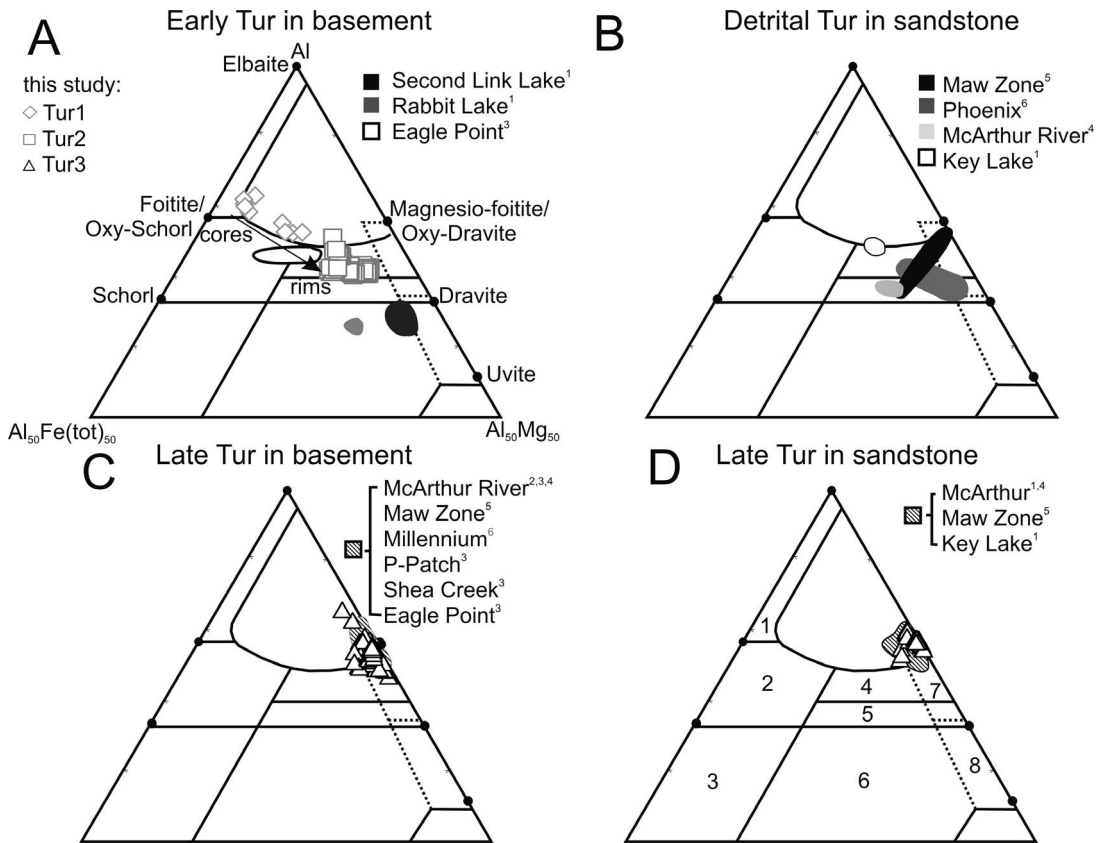
FIG. 6. Tourmaline provenance diagrams of Henry & Guidotti (1985) comparing the composition of tourmaline in the basement and sandstone of the McArthur River mine (this study) with other uranium deposits in the Athabasca Basin. (A) Comparison of early-formed tourmalines in sub-Athabasca crystalline basement rocks. (B) Reported compositions of detrital tourmaline of the Athabasca Group sandstone. (C) Comparison of late-formed, hydrothermal tourmalines in sub-Athabasca crystalline basement rocks. (D) Comparison of late-formed, hydrothermal tourmalines in sandstones. References: (1) Rosenberg & Foit (2006); (2) Kotzer 1993; (3) Mercadier *et al*. (2012); (4) Ng (2012); (5) Quirt *et al*. (1991); and (6) Dann, unpublished data. The numbered fields (shown in D) correspond to host-rock types (after Henry & Guidotti 1985): (l) Li-rich granitoid pegmatites and aplites, (2) Li-poor granitoids and their associated pegmatites and aplites, (3) Fe^{3+}-rich quartz-tourmaline rocks (hydrothermally altered granites), (4) metapelites and metapsammites coexisting with an Al-saturating phase, (5) metapelites and metapsammites not coexisting with an Al-saturating phase, (6) Fe^{3+}-rich quartz-tourmaline rocks, calc-silicate rocks, and metapelites, (7) low-Ca metaultramafics and Cr, V-rich metasediments, and (8) metacarbonates and meta-pyroxenites.

Republic, but it is not common and the oxy-dravite of this study is Mg-rich. The occurrence of zoned oxy-dravite grains, with cores of Tur1/oxy-schörl (Fig. 3A), within pegmatite suggests that oxy-dravite (Tur2) crystallized after peak metamorphism and solidification of partial melts. Furthermore, the oxy-dravite was not observed in the least-altered metamorphic or pegmatitic rocks outside of the P2 fault (Adlakha *et al*. 2014, this study). These observations suggest that oxy-dravite crystallized later along the P2 fault, but before the deposition of the Athabasca Basin.

Mercadier *et al*. (2012) has shown similar B isotope composition of the cores and rims of zoned dravite. The isotopic signature may suggest crystallization during the same event, possibly retrogression. Retrogression is consistent with the replacement of biotite with Fe-Mg chlorite and feldspar with illite, as observed in the oxy-dravite mineral assemblage. However, this interpretation is not consistent with the high X_{Mg} of the tourmaline. The X_{Mg} values of tourmaline commonly reflect temperatures, with retrogression products having lower X_{Mg} than the peak

metamorphic products. For example, Van Hinsberg & Schumacher (2011) confirmed that in the Haut-Allier metamorphic suite, Massif Central, France, dravite formed during peak metamorphism, around early schörlitic cores, and was later rimmed by schörl during retrogression.

It has been suggested that a significant hydrothermal event occurred after the peak metamorphism and prior to the deposition of the Athabasca sandstones (Card 2012, 2014). Movement of faults likely provided conduits for focused fluids along graphitic pelite, and produced pyrite and quartz along major basement structures. The hydrothermal fluids are considered to be responsible for the formation of anomalous quartz-rich rocks, such as silicified pegmatite and "quartzite ridges", in proximity to major basement faults (Card 2012, 2014). It is likely that Tur2 crystallized with quartz and pyrite during this hydrothermal event. The crystallization of Tur2 with pyrite is consistent with relatively low Fe contents in Tur2, as the pyrite would preferentially incorporate Fe.

Origin of magnesio-foitite (Tur3)

It is noted here that tourmaline associated with uranium deposits in the Athabasca Basin has been commonly referred to as dravite, alkali-free dravite, or alkali-deficient dravite in the literature (e.g., Quirt et al. 1991, Kotzer & Kyser 1995, Fayek & Kyser 1997, Jefferson et al. 2007). The compositions of these previously reported tourmalines plot near magnesio-foitite in the provenance diagram (Figs. 4C, D).

The timing of hydrothermal tourmaline with respect to uranium mineralization of the Athabasca Basin has been commonly debated (e.g., Hoeve & Sibbald 1978, Kotzer & Kyser 1995, Fayek & Kyser 1997, Derome et al. 2005, Cloutier et al. 2009, Mercadier et al. 2012, Ng 2012). The composition of magnesio-foitite in this study is similar to the hydrothermal tourmaline reported from other Athabasca uranium deposits (Figs. 4, 6), including Rabbit Lake, Second Link Lake, Key Lake, and Phoenix (Kotzer 1993, Rosenberg & Foit 2006, Mercadier et al. 2012, Ng 2012) and from the REE-rich Maw Zone (Quirt et al. 1991). Magnesio-foitite occurring in quartz veins near the McArthur River Zone 4 ore body was suggested to be a pre-ore alteration by Ng et al. (2013) because it is overprinted by ore-related chlorite. Derome et al. (2005) suggested that magnesio-foitite was synchronous with ore formation, as it is associated with desilicification and occurs in the matrix of ore-hosting breccias. Other evidence supporting a syn-ore crystallization of magnesio-foitite is (1) close spatial association with ore (Hoeve & Sibbald 1978, Kotzer & Kyser 1995, Fayek & Kyser 1997, Derome et al.

2005), and (2) δD and δ^{18}O values of magnesio-foitite, which suggest it formed from the mixing of basinal and basement fluids during mineralization (Kotzer & Kyser 1995). Magnesio-foitite has also been suggested as a post-ore alteration because of its occurrence in voids "created by pre-ore alteration but not filled with uraninite" (Alexandre et al. 2005) and it overprints pre-ore and syn-ore alteration assemblages (Cloutier et al. 2009).

The P2 fault is characterized by alteration forming magnesio-foitite, florencite, sudoite, and illite. Magnesio-foitite is disseminated within these alteration minerals and grain boundaries show no reaction rim (e.g., Fig. 3F), suggesting their equilibrium. Sudoite and illite are widely considered as syn-ore alteration minerals (e.g., Jefferson et al. 2007 and references therein). The assemblage of magnesio-foitite with sudoite, illite, and florencite is especially prevalent around the Zone 2 ore body. In ore zone breccias, the assemblage occurs with uraninite of the main mineralization event. This assemblage is locally overprinted by remobilized uraninite and sudoite (Fig. 3E, F, H). The uraninite formed during the main event and the late recrystallized uraninite are easily differentiated because the compositions are different; the recrystallization product contains high Si, Ca, and Pb, which is similar to the late secondary uraninite reported by Fayek & Kyser (1997). The composition of uraninite and textural evidence suggest that magnesio-foitite and the main-stage uraninite are contemporaneous. Therefore, the results of this study are in agreement with the prevailing interpretation of magnesio-foitite crystallizing from uraniferous fluids during the main-stage mineralization.

Significance of X-site vacancy

The X-site of tourmaline accommodates alkalis and Ca^{2+}, and can be partially vacant. The calculated mineral formula of magnesio-foitite indicates a consistently large X-site vacancy (Fig. 7; Table 3). The abundance of illite suggests reasonably high K$^+$ in the hydrothermal fluids, yet the tourmaline does not contain significant K (<0.01 apfu). Although the X-site may accommodate alkalis, the ionic radius of K$^+$ is too large to replace Na$^+$ and Ca^{2+}. The rarity of K-rich tourmaline is considered to be due to the incompatibility of K$^+$ with the crystal structure of tourmaline and significant K in tourmaline is only reported in ultra high-pressure metamorphic rocks and rocks in close association with evaporites where the K substitutes at the X-site in povondraite (Fe^{3+}-rich tourmaline) (e.g., Bačík et al. 2008, Berryman et al. 2015).

Previous workers have described two fluids during uranium mineralization: (1) an earlier formed NaCl-
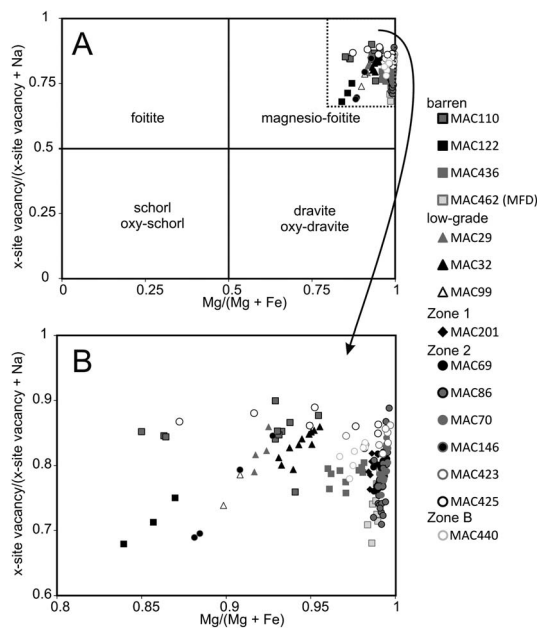
FIG. 7. Binary diagrams of Tur3 data, Mg/(Mg + Fe) *versus* X-site vacancy/(X-site vacancy + Na *apfu*), showing the alkali-deficiency of Tur3. Diagram B shows a smaller range and therefore a larger amount of detail than diagram A. Data of Tur3 from unmineralized areas are represented by squares, from low-grade areas by triangles, from Zone 1 by diamonds, and from Zones 2 and B by circles. Tur3 from Zones 2 and B samples that contain uraninite are represented by open circles.

rich, uranium-bearing brine and (2) an evolved $CaCl_2$-rich brine which formed by the interaction of the earlier brine with basement rocks (Derome *et al.* 2005, Richard *et al.* 2010, Richard *et al.* 2011). Experimental work by von Goerne *et al.* (2001) indicates that Na-deficient tourmaline primarily reflects low X_{Na} of the fluid. Therefore, the low Na^+ contents in tourmaline associated with the Athabascan uranium deposits is surprising if the tourmaline formed from the NaCl-rich fluid. However, von Goerne *et al.* (2001) also demonstrated that the X-site vacancy increases with decreasing temperatures. Uranium deposits of the Athabasca Basin are considered to have formed at low temperatures (<200 °C; *e.g.*, Kotzer & Kyser 1995). Therefore, it is possible that these low temperatures facilitated the formation of magnesio-foitite in lieu of dravite.

It is also possible that magnesio-foitite formed from a $CaCl_2$-rich brine instead of a NaCl-rich brine. This is supported by the lack of Na-bearing phases associated with uranium mineralization, except for magnesio-foitite, which contains very low Na^+ (<0.83

wt.% Na_2O; Table 3). This proposed interpretation is also consistent with the depletion of Na in rocks proximal to the uranium deposits (*e.g.*, Sopuck *et al.* 1983). If this is the case, it is reasonable to question why a Ca-rich tourmaline did not form. Calcium-rich tourmalines, such as uvite and ferruvite, do occur in nature, but their occurrences are rare, restricted to calcareous metasediments and calc-silicate rocks formed at high (>400 °C) temperatures (Henry & Dutrow 1996). Calcium-rich tourmaline has not been reported in rocks formed at low temperatures nor has it been synthesized at low temperatures to date. Experimental work of von Goerne (von Goerne & Franz 2000, von Goerne *et al.* 2001, 2011) found that the X-site vacancy increased with increasing Ca/(Na + Ca) ratio of the fluid (with the exception of pure Ca fluid). Considering that Na preferentially incorporates into tourmaline over Ca, this may explain why magnesio-foitite formed from a $CaCl_2$-rich fluid in lieu of a Ca-bearing tourmaline.

The high X-site vacancy of magnesio-foitite may also be partly attributed to the composition of precursor phases. The rocks in the area were extensively altered before uranium mineralization to form kaolin during weathering of the basement rocks and dickite during diagenesis of the Athabasca Group sandstones. The X-site vacancy of magnesio-foitite is owed to the coupled substitution of $Al + \square = Na + Mg$. High-Al phases such as dickite/kaolinite and sudoite are abundant in the sandstones and basement. Aluminum is not a highly mobile element in low-temperature hydrothermal fluids. The tourmaline likely inherited high Al contents of the precursor minerals, thereby restricting the amount of Na^+ and Ca^{2+} in the mineral's crystal structure. We consider this proposed interpretation the most plausible mechanism explaining high vacancies at the X site.

The role of the P2 fault and origin of the mineral assemblages

In the basement, oxy-dravite and magnesio-foitite occur in close proximity (<50 m) to the P2 fault and are absent in the footwall and hanging-wall of the structure. Oxy-dravite (Tur2) appears evenly distributed along the P2 fault, whereas magnesio-foitite (Tur3) is abundant in the alteration halo of the deposit and sparse in apparently barren areas of the fault. The occurrence of the two distinctly different types of tourmaline along the entire P2 fault reflects different fluids in two separate events before and after the sandstone deposition. This observation suggests that the P2 fault served as a fluid conduit before and after the deposition of Athabasca sandstone. This interpretation is in agreement with those of Card (2014) who
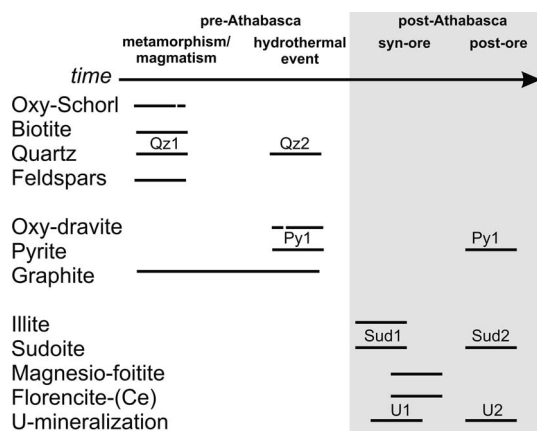
Fig. 8. The paragenesis of mineral assemblages related to tourmaline in the basement rocks along the P2 fault at McArthur River. This figure is modified from Adlakha *et al*. (2014) and incorporates additional data from Adlakha & Hattori (2015).

suggested that multiple events of hydrothermal activity over an extensive period of time, from pre-Athabasca to syn-mineralization, were facilitated by basement structures such as the P2 fault.

The mineral assemblages of tourmaline along the P2 fault attest to multiple fluid events along basement structures (Fig. 8). The earliest assemblage is of oxy-schörl (Tur1) with quartz, plagioclase/feldspar, and biotite. Oxy-dravite (Tur2) then formed with quartz (Qz2), pyrite (Py1), and graphite. An assemblage of magnesio-foitite (Tur3), sudoite (Sud1), illite, and florencite ± uraninite (U1) formed during the main stage of uranium deposition. This assemblage was locally overprinted by remobilized uraninite (U1), sudoite (Sud2), and sulfide (Py2).

The restricted distribution of magnesio-foitite (Tur3) along the P2 fault suggests that B-bearing fluids in the basement were focused along the P2 fault during uranium mineralization. These fluids were likely uraniferous as magnesio-foitite and uraninite are contemporaneous, but uranium deposits only occur in specific areas of the P2 fault (Fig. 1C). Considering the occurrence of magnesio-foitite in both mineralized and barren areas, it is likely that the location of uranium mineralization was dependent upon the supply of a reducing fluid to these sites.

Conclusions

Three types of tourmaline occur in the basement rocks of the P2 fault. Early oxy-schörl (Tur1) crystallized as a primary phase in pegmatite. After peak metamorphism and before deposition of the Athabasca Group sediments, hydrothermal activity along the P2 fault produced oxy-dravite with quartz, graphite, and pyrite. High Mg contents in the oxy-dravite are explained by the removal of Fe by the crystallization of pyrite. After deposition of the Athabasca Group sediments, uraniferous fluids crystallized magnesio-foitite with sudoite, illite, and florencite along the entire P2 fault. The high X-site vacancy of magnesio-foitite is attributed to high Al content in the mineral, which is likely inherited from precursory high-Al phases. This study demonstrates the important role of the P2 fault as the conduit for hydrothermal fluids before and during the uraniferous hydrothermal activity.

References

Adlakha, E.E. & Hattori, K. (2015) Compositional variation and timing of aluminum phosphate-sulfate minerals in the basement rocks along the P2 fault and in association with the McArthur River uranium deposit, Athabasca Basin, Saskatchewan, Canada. *American Mineralogist* **100(7)**, 1386–1399.

Adlakha, E.E., Hattori, K., Zaluski, G., Kotzer, T., & Potter, E.G. (2014) Alteration within the basement rocks associated with the P2 fault and the McArthur River uranium deposit, Athabasca Basin. *Geological Survey of Canada Open File* **7462**, 35 pp.

Alexandre, P., Kyser, K., Polito, P., & Thomas, D. (2005) Alteration mineralogy and stable isotope geochemistry of Paleoproterozoic basement-hosted unconformity-type uranium deposits in the Athabasca Basin, Canada. *Economic Geology* **100(8)**, 1547–1563.

Annesley, I.R., Madore, C., & Portella, P. (2005) Geology and thermotectonic evolution of the western margin of the

Trans-Hudson Orogen: evidence from the eastern sub-Athabasca basement, Saskatchewan. *Canadian Journal of Earth Sciences* **42(4)**, 573–597.

Bačík, P., Uher, P., Sýkora, M., & Lipka, J. (2008) Low-Al tourmalines of the schorl-dravite-povondraite series in redeposited tourmalinites from the Western Carpathians, Slovakia. *Canadian Mineralogist* **46**, 1117–1129.

Bačík, P., Cempírek, J., Uher, P., Novák, M., Ozdín, D., Filip, J., Škoda, R., Breiter, K., Klementová, M., Ďuďa, R., & Groat, L.A. (2013) Oxy-schorl, $Na(Fe^{2+}_2Al)Al_6Si_6O_{18}(BO_3)_3(OH)_3O$, a new mineral from Zlatá Idka, Slovak Republic and Přibyslavice, Czech Republic. *American Mineralogist* **98(2–3)**, 485–492.

Berryman, E.J., Wunder, B., Wirth, R., Rhede, D., Schettler, G., Franz, G., & Heinrich, W. (2015) An experimental study on K and Na incorporation in dravitic tourmaline and insight into the origin of diamondiferous tourmaline from the Kokchetav Massif, Kazakhstan. *Contributions to Mineralogy and Petrology* **169(3)**, 1–16.

Bosi, F. & Skogby, H. (2013) Oxy-dravite, $Na(Al_2Mg)(Al_5Mg)(Si_6O_{18})(BO_3)_3(OH)_3O$, a new mineral species of the tourmaline supergroup. *American Mineralogist* **98(8–9)**, 1442–1448.

Card, C.D. (2012) The Origins of Anomalously Graphitic Rocks and Quartzite Ridges in the Basement to the Southeastern Athabasca Basin. *In* Summary of Investigations 2012, Volume 2. Saskatchewan Geological Survey, Saskatchewan Ministry of the Economy, Miscellaneous Report, 2012-4.2, Paper A-6, 15 pp.

Card, C.D. (2014) Altered Pelitic Gneisses and Associated "Quartzite Ridges" Beneath the Southeastern Athabasca Basin: Alteration Facies and their Relationship to Uranium Deposits along the Wollaston-Mudjatik Transition. *In* Summary of Investigations 2013, Volume 2. Saskatchewan Ministry of the Economy, Miscellaneous Report 2013-4.2, Paper A-4, 23 pp.

Carter, J.D. (1984) Mortimer Hills pegmatite uranium prospect—a Rossing-type uranium deposit in the Gascoyne Province. *Western Australia Geological Survey Report* **12**, 27–31.

Cempírek, J., Stanislav, H., Novák, M., Groat, L., Selway, J., & Šrein, V. (2013) Crystal structure and compositional evolution of vanadium-rich oxy-dravite from graphite quartzite at Bítovánky, Czech Republic. *Journal of Geosciences* **58**, 149–162.

Cloutier, J., Kyser, K., Olivo, G.R., Alexandre, P., & Halaburda, J. (2009) The Millennium uranium deposit, Athabasca Basin, Saskatchewan, Canada: an atypical basement-hosted unconformity-related uranium deposit. *Economic Geology* **104(6)**, 815–840.

Čopjaková, R., Škoda, R., Galiová, M.V., & Novák, M. (2013) Distributions of Y+ REE and Sc in tourmaline and their implications for the melt evolution; examples from NYF pegmatites of the Trebic Pluton, Moldanubian

Zone, Czech Republic. *Journal of Geosciences* **58(2)**, 113–131.

Čopjaková, R., Škoda, R., Galiová, M.V., Novák, M., & Cempírek, J. (2015) Sc-and REE-rich tourmaline replaced by Sc-rich REE-bearing epidote-group mineral from the mixed (NYF+ LCT) Kracovice pegmatite (Moldanubian Zone, Czech Republic). *American Mineralogist* **100(7)**, 1434–1451.

Derome, D., Cathelineau, M., Cuney, M., Fabre, C., Lhomme, T., & Banks, D.A. (2005) Mixing of sodic and calcic brines and uranium deposition at McArthur River, Saskatchewan, Canada: a Raman and laser-induced breakdown spectroscopic study of fluid inclusions. *Economic Geology* **100**, 1529–1545.

Dyar, M.D., Lowe, E.W., Guidotti, C.V., & Delaney, J.S. (2002) Fe^{3+} and Fe^{2+} partitioning among silicates in metapelites: A synchrotron micro-XANES study. *American Mineralogist* **87(4)**, 514–522.

Fayek, M. & Kyser, K. (1997) Characterization of multiple fluid-flow events and rare-earth elements mobility associated with formation of unconformity uranium deposits in the Athabasca basin, Saskatchewan. *Canadian Mineralogist* **35**, 627–658.

Gadas, P., Novák, M., Staněk, J., Filip, J., & Vašinová Galiová, M. (2012) Compositional evolution of zoned tourmaline crystals from pockets in common pegmatites, the Moldanubian Zone, Czech Republic. *Canadian Mineralogist* **50**, 895–912.

Hajnal, Z., Pandit, B., Reilkoff, B., Takacs, E., Annesley, I., & Wallster, D. (2007) Recent development in 2D and 3D seismic imaging of high-grade uranium ore deposit related environments, in the Eastern Athabasca Basin, Canada. *In* Exploration in the new millennium (B. Milkereit, ed.). Proceedings of the Fifth Decennial International Conference on Mineral Exploration, 1131–1135.

Hawthorne, F.C. & Dirlam, D.M. (2011) Tourmaline the indicator mineral: From atomic arrangement to Viking navigation. *Elements* **7(5)**, 307–312.

Henry, D.J. & Dutrow, B.L. (1996) Metamorphic tourmaline and its petrologic applications. *In* Boron: Mineralogy, Petrology and Geochemistry (E.S. Grew & L.M. Anovitz, eds.). *Reviews in Mineralogy* **33**, 503–557.

Henry, D.J. & Guidotti, C.V. (1985) Tourmaline as a petrogenetic indicator mineral – An example from the staurolite-grade metapelites of NW Maine. *American Mineralogist* **70(1–2)**, 1–15.

Henry, D.J., Novák, M., Hawthorne, F.C., Ertl, A., Dutrow, B.L., Uher, P., & Pezzotta, F. (2011) Nomenclature of the tourmaline-supergroup minerals. *American Mineralogist* **96(5–6)**, 895–913.

Hoeve, J. & Quirt, D. (1984) Mineralization and host rock alteration in relation to clay mineral diagenesis and evolution of the middle-Proterozoic, Athabasca Basin,

northern Saskatchewan, Canada. *Saskatchewan Research Council (SRC) Technical Report* **187**, 187 pp.

HOEVE, J. & SIBBALD, T.I. (1978) On the genesis of Rabbit Lake and other unconformity-type uranium deposits in northern Saskatchewan, Canada. *Economic Geology* **73(8)**, 1450–1473.

JEFFERSON, C.W., THOMAS, D.J., GANDHI, S.S., RAMAEKERS, P., DELANEY, G., BRISBIN, D., CUTTS, C., PORTELLA, P., & OLSON, R.A. (2007) Unconformity-associated uranium deposits of the Athabasca basin, Saskatchewan and Alberta. *In* EXTECH IV: Geology and Uranium EXploration TECHnology of the Proterozoic Athabasca Basin, Saskatchewan and Alberta. *Geological Survey of Canada Bulletin* **588**, 2367.

KERR, W.C. (2010) The discovery of the Phoenix Deposit; a new high-grade, Athabasca Basin unconformity-type uranium deposit, Saskatchewan, Canada. *Society of Economic Geologists Special Publications* **15**, 703–728.

KOTZER, T.G. (1993) *Fluid History of the Proterozoic Athabasca Basin*. Unpublished Ph.D. Thesis, University of Saskatchewan, Saskatoon, Saskatchewan, 290 pp.

KOTZER, T.G. & KYSER, T.K. (1995) Petrogenesis of the Proterozoic Athabasca Basin, northern Saskatchewan, Canada, and its relation to diagenesis, hydrothermal uranium mineralization and paleohydrogeology. *Chemical Geology* **120(1)**, 45–89.

KYSER, K., HIATT, E., RENAC, C., DUROCHER, K., HOLK, G., & DECKART, K. (2000) Diagenetic fluids in Paleo- and Meso-Proterozoic sedimentary basins and their implications for long protracted fluid histories. *In* Fluids and basin evolution (T.K. Kyser, ed.). *Mineralogical Association of Canada Short Course* **28**, 225–262.

LEWRY, J.F. & SIBBALD, T. (1980) Thermotectonic evolution of the Churchill province in northern Saskatchewan. *Tectonophysics* **68**, 45–82.

MACDONALD, C. (1985) Mineralogy and geochemistry of the sub-Athabasca regolith near Wollaston Lake. *Geology of Uranium Deposits: Canadian Institute of Mining and Metallurgy Special* **32**, 155–158.

MCGILL, B., MARLATT, J., MATTHEWS, R., SOPUCK, V., HOMENIUK, L., & HUBREGTSE, J. (1993) The P2 North uranium deposit Saskatchewan, Canada. *Exploration Mining Geology* **2(4)**, 321–333.

MERCADIER, J., RICHARD, A., & CATHELINEAU, M. (2012) Boron-and magnesium-rich marine brines at the origin of giant unconformity-related uranium deposits: $\delta^{11}B$ evidence from Mg-tourmalines. *Geology* **40(3)**, 231–234.

NG, R. (2012) *Geochemical and mineralogical evolution of the McArthur River Zone 4 unconformity-related uranium ore body and application of iron oxidation state in clay alteration as indicator of uranium mineralization*. Unpublished M.Sc. thesis, Queen's University, Kingston, Ontario, Canada, 207 pp.

NG, R., ALEXANDRE, P., & KYSER, K. (2013) Mineralogical and Geochemical Evolution of the Unconformity-Related McArthur River Zone 4 Orebody in the Athabasca Basin, Canada: Implications of a Silicified Zone. *Economic Geology* **108(7)**, 1657–1689.

NOVÁK, M., POVONDRA, P., & SELWAY, J.B. (2004) Schorl-oxy-schorl to dravite-oxy-dravite tourmaline from granitic pegmatites; examples from the Moldanubicum, Czech Republic. *European Journal of Mineralogy* **16**, 323–333.

PAL, D., TRUMBULL, R., & WIEDENBECK, M. (2010) Chemical and boron isotope compositions of tourmaline from the Jaduguda U (–Cu–Fe) deposit, Singhbhum shear zone, India: Implications for the sources and evolution of mineralizing fluids. *Chemical Geology* **27**, 245–260.

QUIRT, D., KOTZER, T., & KYSER, T.K. (1991) Tourmaline, phosphate minerals, zircon and pitchblende in the Athabasca Group: Maw Zone and McArthur River areas. Saskatchewan: Summary of Investigations 1991, *Saskatchewan Geological Survey Miscellaneous Report* **91(4)**, 11 pp.

RAMAEKERS, P., JEFFERSON, C.W., YEO, G.M., COLLIER, B., LONG, D.G.F., DREVER, G., MCHARDY, S., JIRICKA, D., CUTTS, C., WHEATLEY, K., CATUNEAU, O., BERNIER, S., KUPSCH, B., & POST, R.T. (2007) Revised geological map and stratigraphy of the Athabasca Group, Saskatchewan and Alberta. *In* EXTECH IV: Geology and Uranium EXploration TECHnology of the Proterozoic Athabasca Basin, Saskatchewan and Alberta. *Geological Survey of Canada Bulletin* **588**, 155–192.

RICHARD, A., PETTKE, T., CATHELINEAU, M., BOIRON, M.C., MERCADIER, J., CUNEY, M., & DEROME, D. (2010) Brine–rock interaction in the Athabasca basement (McArthur River U deposit, Canada): consequences for fluid chemistry and uranium uptake. *Terra Nova* **22(4)**, 303–308.

RICHARD, A., BANKS, D.A., MERCADIER, J., BOIRON, M.C., CUNEY, M., & CATHELINEAU, M. (2011) An evaporated seawater origin for the ore-forming brines in unconformity-related uranium deposits (Athabasca Basin, Canada): Cl/Br and $\delta^{37}Cl$ analysis of fluid inclusions. *Geochimica et Cosmochimica Acta* **75(10)**, 2792–2810.

RICHARD, A., ROZSYPAL, C., MERCADIER, J., BANKS, D.A., CUNEY, M., BOIRON, M.C., & CATHELINEAU, M. (2012) Giant uranium deposits formed from exceptionally uranium-rich acidic brines. *Nature Geoscience* **5(2)**, 142–146.

ROSENBERG, P.E. & FOIT, F.F. (2006) Magnesio-foitite from the uranium deposits of the Athabasca Basin, Saskatchewan, Canada. *Canadian Mineralogist* **44(4)**, 959–965.

SOPUCK, V.J., DECARLA, A., WRAY, E.M., & COOPER, B. (1983) The application of lithogeochemistry in the search for unconformity-type uranium deposits, Northern Saskatchewan, Canada. *Journal of Geochemical Exploration* **19**, 77–99.

van Hinsberg, V.J. & Schumacher, J.C. (2011) Tourmaline as a petrogenetic indicator mineral in the Haut-Allier metamorphic suite, Massif Central, France. *Canadian Mineralogist* **49(1)**, 177–194.

von Goerne, G. & Franz, G. (2000) Synthesis of Ca-tourmaline in the system CaO–MgO–Al_2O_3–SiO_2–B_2O_3–H_2O–HCl. *Mineralogy and Petrology* **69(3–4)**, 161–182.

von Goerne, G., Franz, G., & Heinrich, W. (2001) Synthesis of tourmaline solid solutions in the system Na_2O–MgO–Al_2O_3–SiO_2–B_2O_3–H_2O. *Contributions to Mineralogy and Petrology* **141(2)**, 160–173.

von Goerne, G., Franz, G., & van Hinsberg, V.J. (2011) Experimental determination of Na–Ca distribution between tourmaline and fluid in the system CaO–Na_2O–MgO–Al_2O_3–SiO_2–B_2O_3–H_2O. *Canadian Mineralogist* **49(1)**, 137–152.